Available online at www.sciencedirect.com
ScienceDirect
Trans. Nonferrous Met. Soc. China 32(2022) 233−250
Transactions of Nonferrous Metals Society of China
www.tnmsc.cn

$Ti_3C_2T_x$ MXene doped by W atoms for full-spectrum photofixation of nitrogen

Qi LI[1#], Ji-liang XU[1#], San-mei WANG[1], Kai-fu YU[2], Wen-kun ZHU[2], Ting-ting HOU[1], Lan-tian ZHANG[1], Wen-hua ZHANG[3], Shu-quan LIANG[1], Liang-bing WANG[1]

1. School of Materials Science and Engineering, Central South University, Changsha 410083, China;
2. State Key Laboratory of Environment-friendly Energy Materials, Southwest University of Science and Technology, Mianyang 621010, China;
3. CAS Key Laboratory of Materials for Energy Conversion, Department of Materials Science and Engineering, University of Science and Technology of China, Hefei 230026, China

Received 11 January 2021; accepted 25 August 2021

Abstract: Full-spectrum photofixation of N_2 with remarkable NH_3 production rate of 228 μmol/(g·h) was achieved by W atoms doped $Ti_3C_2T_x$ MXene (W/$Ti_3C_2T_x$-U) catalyst without sacrificial agents at room temperature. The effects of W doping and ultrasonic intercalation of $Ti_3C_2T_x$ MXene were studied. Scanning transmission electron microscope, electron spin resonance spectra, X-ray photoemission spectroscopy, UV-Vis spectrophotometer, temperature programmed adsorption analyzer and density functional theory calculation were used to characterize the obtained catalysts. Results showed that $Ti_3C_2T_x$ MXene harvested ultraviolet-visible and near-infrared light to generate hot electrons. In addition, the doped W atoms played an effective role in adsorbing and activating N_2 molecules by donating electrons to the anti-bonding orbital of N_2 molecules to elongate the bond length of N≡N.
Key words: nitrogen fixation; photocatalysis; MXene; tungsten; full-spectrum

1 Introduction

Ammonia (NH_3) is one of the most significant chemical products in modern society, as the fertilizer originating from NH_3 directly contributes to sustaining food production for billions of people around the world. Due to the inertness of nitrogen molecules (N_2), the reduction of N_2 by H_2 over iron-based catalysts through Haber-Bösch process is among the biggest energy hogs in chemical industry, consuming ~2% of the world's annual energy supply [1,2]. Photofixation of N_2 in water paves a novel avenue to environmentally friendly production of NH_3 by using natural sunlight as the driving force. Owing to the diligent efforts of a variety of researchers, semiconductors and hybrid materials have been successfully applied in N_2 photoreduction [3−11]. In order to simultaneously reduce N_2 and oxidize H_2O, the conductor band (CB) of semiconductors is thermodynamically required to locate more negative than the reduction potential of N_2 ($\varphi^{\ominus}(N_2/NH_3)$=−0.05 V (vs NHE)), while the valence band (VB) should locate more positive than the oxidation potential of H_2O ($\varphi^{\ominus}(H_2O/O_2)$=1.23 V (vs NHE)) [12,13]. Accordingly, only the part of sunlight with enough photonic energy to overcome band gap is able to be efficiently harvested by semiconductors towards the N_2 photoreduction (Fig. 1(a)). In order to elevate the utilization efficiency of sunlight, building partial occupied band (POB) by introducing foreign atoms is an

Corresponding author: Liang-bing WANG, Tel: +86-15856964781, E-mail: wanglb@csu.edu.cn
[#]Qi LI and Ji-liang XU contributed equally to this work
DOI: 10.1016/S1003-6326(21)65790-4

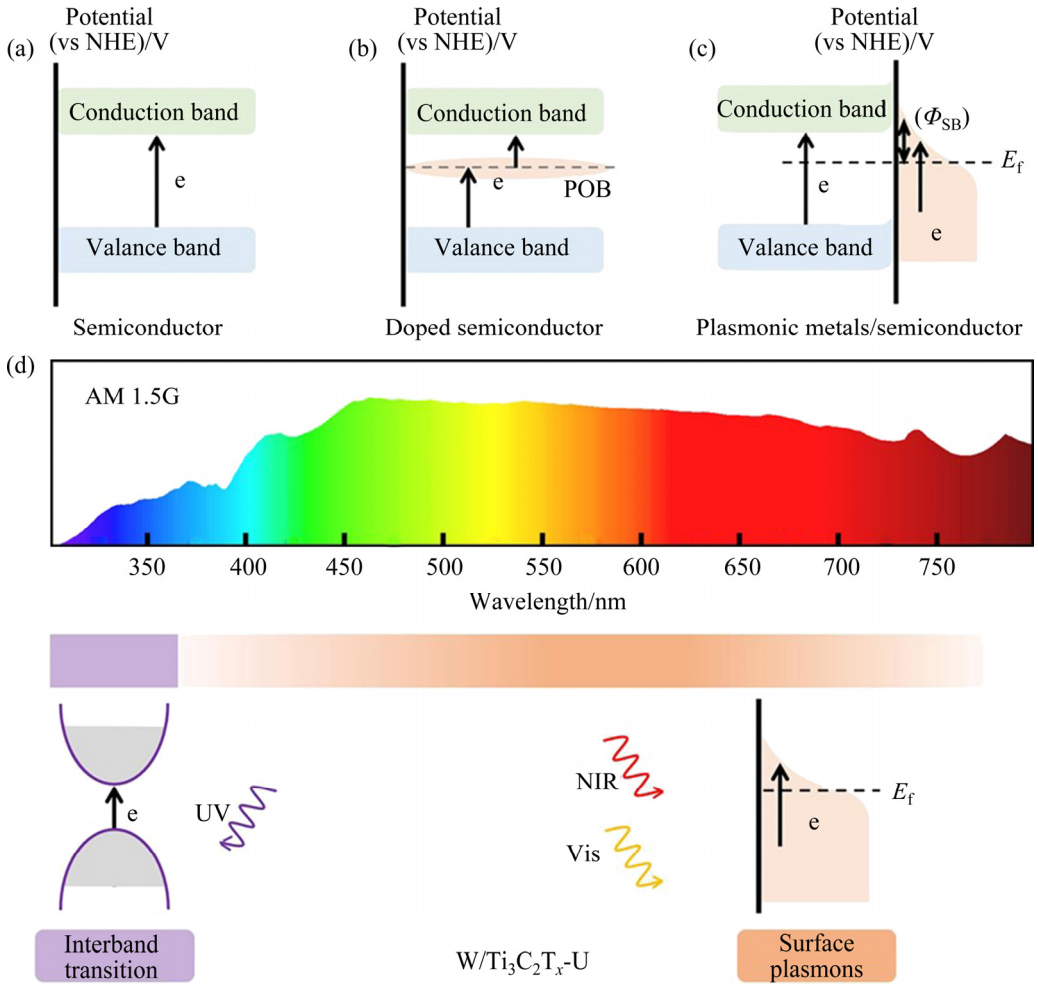

Fig. 1 Schematic illustration of electronic structures of semiconductors (a), doped semiconductors with POB (b), plasmonic metals/semiconductor hybrid materials (c), and W/$Ti_3C_2T_x$-U (d) (Due to the quality of both ultrathin two-dimensional and plasmonic materials, W/$Ti_3C_2T_x$-U realized full-spectrum responses of light)

attractive strategy (Fig. 1(b)). The POB enables both the VB-to-POB and POB-to-CB transitions, allowing the photo-excitation by the photons with energy lower than the bandgap [14,15]. Unfortunately, POB also serves as a recombination site for photo-generated electron-hole pairs to reduce the separation efficiency of electron-hole pairs. Besides, electron localization by the states of POB also leads to additional thermal activation for the transition process, further reducing the possibility of POB-to-CB transition [16−19]. Construction of hybrid materials is another strategy to realize full-spectrum photofixation of N_2. For example, integration of the semiconductor with plasmonic metals (e.g., Au, Ag and Cu nanocrystals) efficiently extends the spectral range of harvesting sunlight in N_2 photofixation [20−24]. Although hot electrons are generated over plasmonic metals, the existence of Schottky barrier between plasmonic metals and semiconductors hampers the transformation of hot electrons from plasmonic metals to semiconductors (Fig. 1(c)) [25−27]. Therefore, developing highly active photocatalysts to realize full-spectrum photofixation of N_2 is urgently desired but challenging.

Serving as a new family of two-dimensional transition metal carbides, carbonitrides, and nitrides, MXenes have attracted tremendous attention due to their excellent performance in renewable energy applications. Interestingly, MXenes have been recently discovered to exhibit impressive optical and plasmonic properties associated with their ultrathin-atomic-layer structure [28−30]. In particular, $Ti_3C_2T_x$ MXene (T stands for the surface termination groups like —OH, —F, and —O, etc.) exhibits impressed plasmonic property in Vis-NIR region theoretically and experimentally [31−34]. Due to the quality of two-dimensional and

plasmonic materials, MXenes are potential candidates for full-spectrum photocatalysts towards N_2 photofixation by integration of highly active sites.

Herein, we successfully realized full-spectrum photofixation of N_2 with remarkable catalytic activity by doping W atoms into $Ti_3C_2T_x$ MXene ($W/Ti_3C_2T_x$-U). Ultraviolet-NIR (UV-NIR) light is harvested by $Ti_3C_2T_x$ MXene to generate hot carriers, while N_2 molecules are adsorbed and activated on the W atom sites (Fig. 1(d)). Impressively, an excellent NH_3 production rate of 228 μmol/(g·h) in pure water at room temperature (RT) was achieved by $W/Ti_3C_2T_x$-U under UV-NIR light irradiation. Further mechanistic studies revealed that doped W atoms directly promoted the adsorption and activation of N_2 molecules by donating electrons to the anti-bonding orbital of N_2 molecules to elongate the bond length of N≡N.

2 Experimental

2.1 Materials and chemicals

W, Al powders, Nessler's reagent, hydrofluoric acid (HF, ≥40%), dimethyl sulfoxide (DMSO) and potassium sodium tartrate (PST) were purchased from Sinopharm Chemical Reagent Co., Ltd. Sodium nitroprusside, sodium citrate, NaOH, phenol, methanesulfonic acid, TiC, and TiH_2 powders were obtained from Shanghai Macklin Biochemical Co., Ltd. Commercial Cu-SSZ-13 zeolite catalyst was obtained from Kaite Co., Ltd. in Tianjin, China. The high purity argon (Ar, ≥99.999%) and high purity nitrogen (N_2, ≥99.999%) were ordered from Saizhong Specail Gas Co., Ltd. All aqueous solutions were prepared using ultrapure water with a resistivity of 18.2 MΩ·cm. All solvents and chemicals are analytically pure.

2.2 Preparation of Ti_3AlC_2 and W/Ti_3AlC_2

Ti_3AlC_2 powder was synthesized by mixing 7.484 g of TiC powder, 3.118 g of TiH_2 powder, and 1.855 g of Al powder (the molar ratio of TiC:TiH_2:Al was 2:1:1.1) for 10 h in a ball mill at the speed of 600 r/min. The mixed powders were then heated in a high temperature atmosphere resistance furnace to 1400 °C with a heat-up speed of 5 °C/min under a flow of Ar, followed by maintaining at 1400 °C for 2 h and then furnace cooling to RT [35]. Then the obtained Ti_3AlC_2 block was ground to pass through a 38 μm sieve to gain Ti_3AlC_2 powder. The preparation method of W/Ti_3AlC_2 powder was similar to that of Ti_3AlC_2 powder, except that W powder was added and the amount of TiH_2 powder was reduced during the ball milling process. In a typical synthesis procedure, W/Ti_3AlC_2 powder was synthesized by mixing 7.484 g of TiC powder, 2.931 g of TiH_2 powder, 0.690 g of W powder and 1.855g of Al powder (the molar ratio of TiC:TiH_2:W:Al was 2:0.94:0.06:1.1) in a ball mill. The ball milling time and ball milling speed are consistent with the preparation process of Ti_3AlC_2. Then the mixed W/Ti_3AlC_2 precursor powder was also heated to 1400 °C with a heat-up speed of 5 °C/min under a Ar flow in a high temperature atmosphere resistance furnace and kept at 1400 °C for 2 h, then cooled to RT in the furnace. Finally, the W/Ti_3AlC_2 powder was obtained by grinding the W/Ti_3AlC_2 block to pass through a 38 μm sieve. The as-synthesized Ti_3AlC_2 powder was characterized by X-ray diffraction (XRD), all the diffraction peaks confirmed the formation of pure Ti_3AlC_2 phase (PDF No. 52−0875). The XRD pattern of W/Ti_3AlC_2 powder was the same as that for Ti_3AlC_2 powder (Fig. 2).

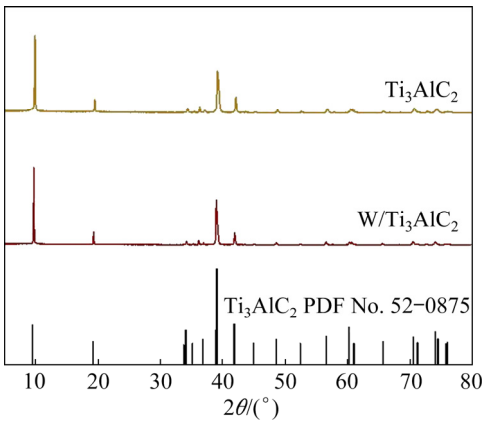

Fig. 2 XRD patterns of Ti_3AlC_2 and W/Ti_3AlC_2

2.3 Preparation of $Ti_3C_2T_x$-NU, $W/Ti_3C_2T_x$-NU, $Ti_3C_2T_x$-U and $W/Ti_3C_2T_x$-U

Al species in Ti_3AlC_2 and W/Ti_3AlC_2 powders were selectively etched by immersing 2.0 g of Ti_3AlC_2 or W/Ti_3AlC_2 powders in 30 mL HF solution, and then magnetic stir at RT for 20 h. After that, the suspension liquid was centrifuged and washed with ultrapure water utill the pH rose to 6.0. Subsequently, the etched powders were centrifugally seperated and dried under vacuum at

80 °C for 8 h to obtain $Ti_3C_2T_x$-NU (NU: not ultrasonicated in DMSO) and W/$Ti_3C_2T_x$-NU, respectively. In a typical synthesis procedure for $Ti_3C_2T_x$-U (U: ultrasonicated in DMSO) and W/$Ti_3C_2T_x$-U, the obtained $Ti_3C_2T_x$-NU and W/$Ti_3C_2T_x$-NU powders were immersed respectively in 30 mL of DMSO and magnetic stirred at RT for 24 h, then sonicated for 2 h. Subsequently, the as-obtained powders were washed and collected by suction filtration with ethyl alcohol and water. Finally, the filtered products were vacuum dried at 80 °C for 8 h to gain $Ti_3C_2T_x$-U and W/$Ti_3C_2T_x$-U, respectively. Figure 3 showed the XRD patterns of $Ti_3C_2T_x$-NU, $Ti_3C_2T_x$-U, W/$Ti_3C_2T_x$-NU and W/$Ti_3C_2T_x$-U. The XRD pattern of W/$Ti_3C_2T_x$-U MXenes was quite similar to that of $Ti_3C_2T_x$-U MXenes, indicating that no new crystalline phase was generated during whole synthetic process after doping W atoms. In addition, the XRD peaks of the treated $Ti_3C_2T_x$-U and W/$Ti_3C_2T_x$-U were all shifted to lower angles corresponding to higher cell parameter *c*.

2.4 Elimination of NO_x in catalyst and raw gas

In order to eliminate nitrate (NO_3^-) or nitrite (NO_2^-) from obtained catalysts and raw gas, and to further verify the origin of the ammonia, we conducted purification experiments over catalyst and raw gas [36,37]. All the obtained catalysts were purified by annealing in a tubular furnace under Ar atmosphere at 500 °C for 4 h [38]. The elimination containing nitrogen in the raw $^{14}N_2$, $^{15}N_2$ and Ar gas was performed in a fixed bed reactor. Typically, 5 g of commercial Cu-SSZ-13 catalyst was put into the reactor. The system was then heated to 350 °C with a heating rate of 10 °C/min and kept at 350 °C with a $^{14}N_2$, $^{15}N_2$ or Ar flow rate of 30 mL/min [39]. The purified gas was collected for further detection or reaction via the gas outlet of the fixed bed reactor.

2.5 Detection of NO_x species

To begin with nitrate (NO_3^-) or nitrite (NO_2^-) ion, standard curves were calibrated by ion chromatograph method through a series of KNO_3 or KNO_2 solution with incremental concentration of 0, 0.05, 0.1, 0.2, 0.3, 0.4, 0.5, 1, 1.5, and 2 μg/mL. In the NO_3^- or NO_2^- ion detecting process, 0.24 mol/L of sodium carbonate solution and 0.3 mol/L of sodium bicarbonate solution were used as the anion eluent solution with a flow rate of 1 mL/min. The self-regenerating suppressor (SRS) current was set to be 36 mA and the chromatographic column temperature was kept at 35 °C. In order to calibrate the peak area vs concentration profile, 0.15 mL of standard KNO_3 or KNO_2 solution was injected into an ion chromatograogy through the 25 μL quantitative injection loop to acquire analyte peak for NO_x anions. Based on the obtained chromatograms, we plotted the profile of peak areas vs NO_3^- or NO_2^- anion concentration of standard KNO_3 or KNO_2 solution. Linear correlations with R^2=0.998 and R^2=0.999 were obtained for NO_3^- and NO_2^-, respectively (Fig. 4).

To quality the NO_3^- and NO_2^- in the obtained catalyst, 10 mg of catalysts were added into 10 mL of ultrapure water and magnetically stirred for 30 min. Subsequently the catalysts were removed from the liquid sample using a disposable syringe filter. Then 0.15 mL of filtrate was injected into an ion chromatograogy. No NO_x ions were detected on purified catalysts.

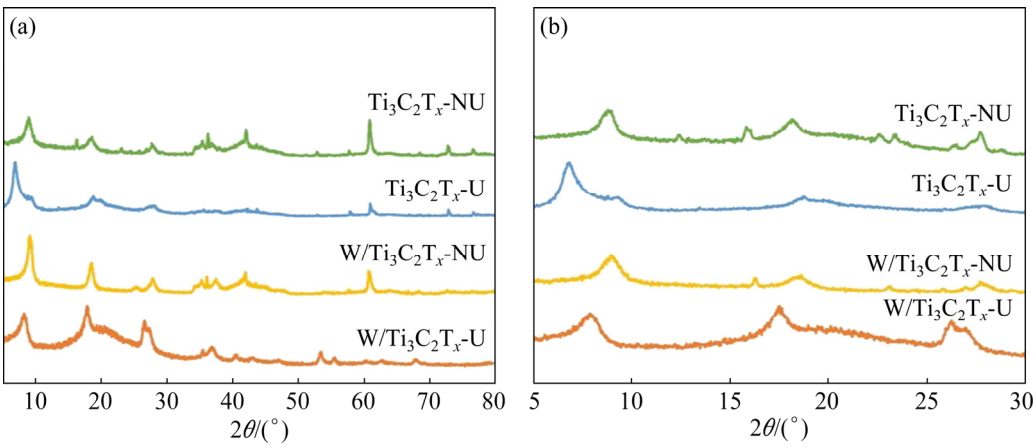

Fig. 3 XRD patterns (a) and magnified XRD patterns (b) of $Ti_3C_2T_x$-NU, $Ti_3C_2T_x$-U, W/$Ti_3C_2T_x$-NU and W/$Ti_3C_2T_x$-U

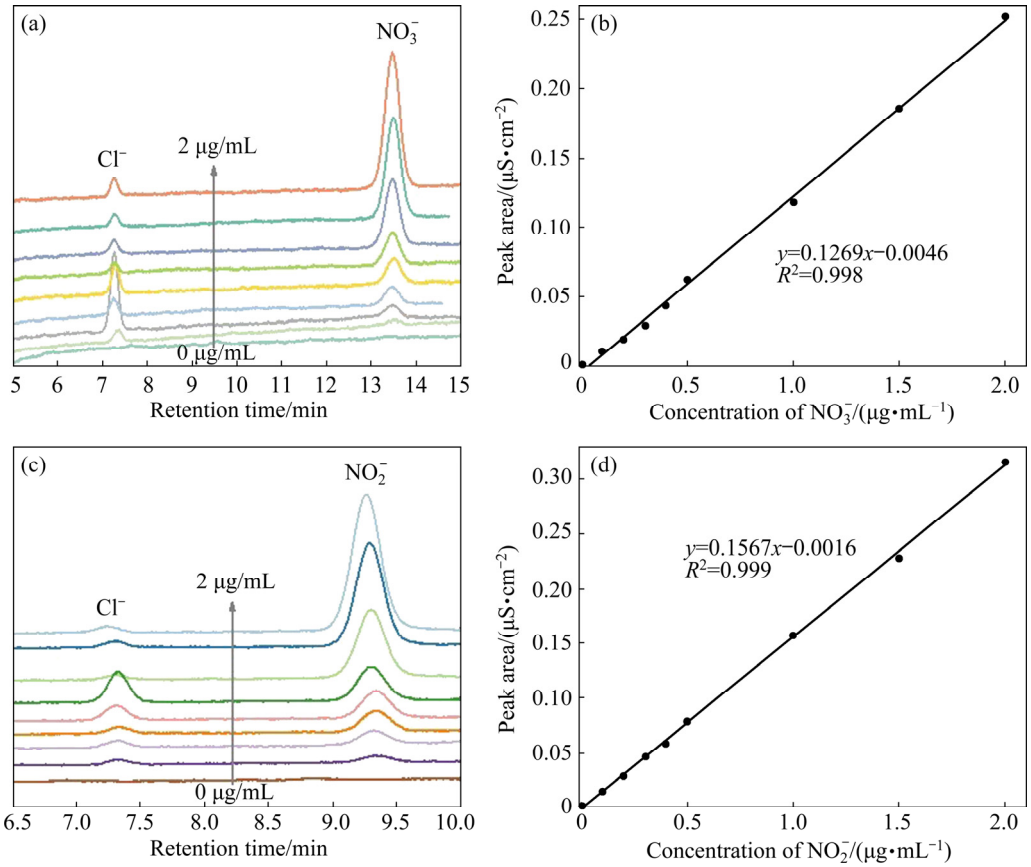

Fig. 4 Spectra of ion chromatography for KNO_3 solution with different concentrations (a), standard curve of concentration vs peak area of NO_3^- in ion chromatography spectra (b), spectra of ion chromatography for KNO_2 solution with different concentrations (c), and standard curve of concentration vs peak area of NO_2^- in ion chromatography spectra (d)

To quality the NO_3^- and NO_2^- in the $^{14}N_2$ and Ar gas, 20 mL of ultrapure water were bubbled with commercial $^{14}N_2$ or Ar at a flow rate of ~30 mL/min for 20 min without any catalysts. Then, 0.15 mL of $^{14}N_2$ or Ar saturated solution was injected into an ion chromatograogy. No NO_x ions were detected in the purified $^{14}N_2$ and Ar gas. As for the identification of NO_3^- and NO_2^- in the $^{15}N_2$, the gas flow rate reduced to ~15 mL/min due to the high cost of $^{15}N_2$. Finally, 0.15 mL of $^{15}N_2$ saturated solution was injected into an ion chromatograogy. No NO_x ions were detected in the purified $^{15}N_2$.

2.6 Photocatalytic tests

All photocatalytic reactions were conducted in a 100 mL glass reaction reactor. In a typical reaction, 20 mL of ultrapure water and 10 mg of purified photocatalysts were added into the reactor. The mixture was sonicated for 5 min to disperse the catalysts evenly in water and then bubbled with purfied N_2 with a flow velocity of ~30 mL/min for 20 min. Subsequently, the mixture was agitated on a magnetic stirrer accompanied by the irradiation of xenon lamp (Perfectlight PLS-SXE300) at 250 mW/cm^2 under full-spectrum. After the reaction was over, the generated NH_3 in the reaction solution was spectrophotometrically analyzed by Nessler's reagent colorimetry. In order to test the stability of W/$Ti_3C_2T_x$-U, the first round of testing was performed as above method. After the reaction, the reaction suspension was immediately filtered with suction. The precipitated catalysts were sonicated with ultrapure water and filtered again with suction. Then, the used catalysts were subjected to go through the next catalytic cycle and repeated the process.

2.7 Nessler's reagent colorimetry

For the estimation of generated ammonia, we calibrated the Nessler's regent standard curve through the Nessler's regent and a series of ammonia solutions with incremental concentration

(0.11, 0.44, 0.66, 0.88, 1.1, 2.2, 3.3, 4.4 and 5.5 μg/mL, respectively). Firstly, 25 g of PST was diluted to 50 mL with ultrapure water by using a volumetric flaskto to obtain PST solution (0.5 g/mL, denoted as PST-0.5). Then, 0.5 mL of PST-0.5 was added into 10 mL of standard ammonia solution. Then, 0.5 mL of Nessler's reagent was injected to the mixture and kept the solution at 25 °C for 30 min. Finally, 3 mL of the mixture solution was taken out into a UV-Vis spetrophptpmeter to test the absorbance intensity at 420 nm (Fig. 5(a)). We plotted the relationship curve between the concentration of standard solution and the absorbance (Fig. 5(b)).

In order to eastimate the generated NH_3 during photocatalytic process, the reaction solution was centrifuged to remove the catalysts, and 0.5 mL of PST-0.5 was added into 10 mL of reaction filtrate, followed by the injection of 0.5 mL of Nessler's reagent to the mixture. The mixture was kept at 25 °C for 30 min, and 3 mL of the mixture solution was taken out into a UV-Vis spectrophotometer to test the absorbance intensity at 420 nm. The ammonia concentration of the reaction solution was obtaind according to the Nessler's regent colorimetry standard curve and the light absorbance at 420 nm.

2.8 Indophenol blue colorimetry

0.5 g of sodium nitroprusside, 2.4 g of NaOH and 14.7 g of sodium citrate were diluted to 49.50, 10.00 and 50.00 mL with ultrapure water to obtain sodium nitroprusside solution (1 wt.%, Solution A), NaOH solution (6.0 mol/L, Solution B) and sodium citrate solution (1.5 mol/L, Solution C), respectively. Then, 3 mL of Solution A, 6.5 mL of Solution B, and 5 mL of phenol solution (6.05 mol/L) were added into 50 mL of Solution C. After magnetic stirring the mixture at RT for 15 min, indophenol blue regent was acquired and stored at 5 °C. Meanwhile, a series of standard ammonia solutions with incremental concentration (0.11, 0.44, 0.66, 0.88, 1.1, 2.2, 3.3, 4.4 and 5.5 μg/mL, respectively) were prepared by dilution method. To calibrate the standard curve for NH_3 detection, 1 mL of NaClO solution (0.05 mol/L) and 1 mL of indophenol blue regent were successively added into 10 mL of standard ammonia solution. The mixture was kept at 25 °C for 30 min, then 3 mL of the mixture solution was taken out into a UV-Vis spectrophotometer to test the absorbance intensity at 641 nm (Fig. 6(a)). Then, we plotted the relationship curve between the concentration of the standard solutions and the absorbance value at 641 nm, where a linear correlation with R^2=0.998 was acquired (Fig. 6(b)).

In order to quantify the NH_3 generated after the reaction, 10 mL of reaction solution after centrifugation to remove catalyst was mixed with 1 mL of NaClO (0.05 mol/L) and 1 mL of indophenol blue regent. After keeping the mixture at 25 °C for 30 min, 3 mL of the coloured solution was drawn out into a UV-Vis spectrophotometer to test the absorbance intensity at 641 nm. The ammonia concentration of the reaction solution was obtained according to the indophenol blue colorimetry standard curve and light absorbance at 641 nm.

2.9 Ion chromatograph method

In the process of detecting NH_4^+, 4.5 mmol/L of methanesulfonic acid was used as the cation eluent solution with a flow rate of 1 mL/min. The self-

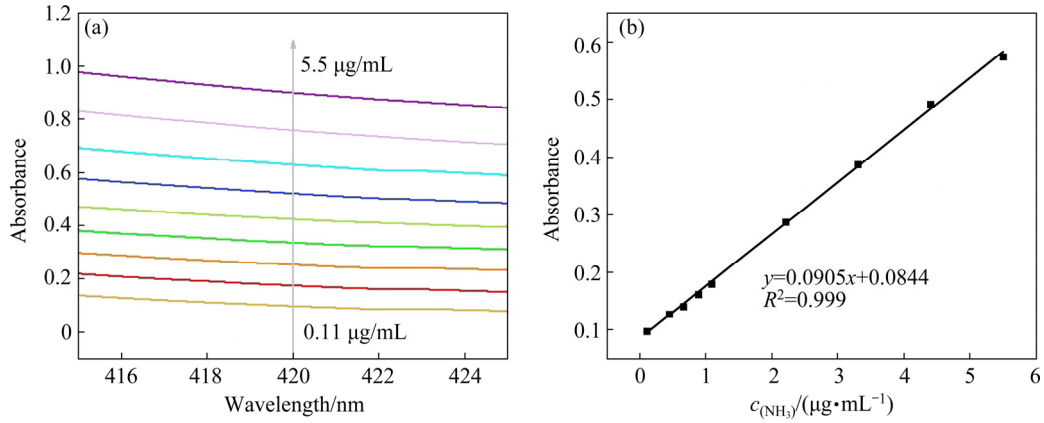

Fig. 5 UV-Vis absorption spectra of ammonia solutions after adding Nessler's reagent (a), and standard curve for NH_3 detection with Nessler's reagent (b)

regenerating suppressor (SRS) current was set to be 75 mA and the chromatographic column temperature was kept at 35 °C. In order to calibrate the peak area vs concentration profile, 0.15 mL of standard NH_4Cl solution with a series of incremental NH_4^+ cations concentration (0.03, 0.05, 0.10 and 0.20 μmol/mL, respectively) was injected into an ion chromatograaogy through the 25 μL quantitative injection loop to acquire analyte peak for NH_4^+ cations (Fig. 7(a)). Based on the obtained chromatograms, we plotted the profile of peak areas vs NH_4^+ concentrations of standard NH_4Cl solution (Fig. 7(b)).

In order to determine the quality of NH_3 generated during the photocatalysis process, we centrifuged the reaction solution to remove the catalysts and used the same method to analyze 25 μL of reaction solution. According to the standard curve and peak areas of detected NH_4^+ cations, the generated ammonia concentration was acquired. It is worth noting that the methanesulfonic acid in cation eluent liquid ensured the transfromation of the NH_3 in the reaction solution to NH_4^+ cation for detecting by ion chromatograph.

2.10 ^{1}H-NMR method

Proton nuclear magnetic resonance (^{1}H-NMR) spectroscopy was also used in the quantification of the genetared NH_3. For the calibration of standard relation curve of concentration vs peak area of ^{1}H-NMR spectrum, 14, 54, 80, 107 and 160 μg of $^{14}NH_4Cl$ were respectively added into a mixture of 20 μL of ultrapure water and 0.6 mL of d_6-DMSO. The obtained samples were measured by ^{1}H NMR spectroscopy. The obtained ^{1}H-NMR (400 MHz) spectra of $^{14}NH_4Cl$ solution with different concentrations were displayed in Fig. 8(a). Then we drew the curve of concentrations of standard solution vs the area of Peak 1 (Fig. 8(b)). For the NH_3 quantitative analysis of the reaction solution, we added 20 mL of uptralpure water and 10 mg of purified photocatalysts into a 100 mL glass reaction reactor. The mixture was sonicated for 5 min to

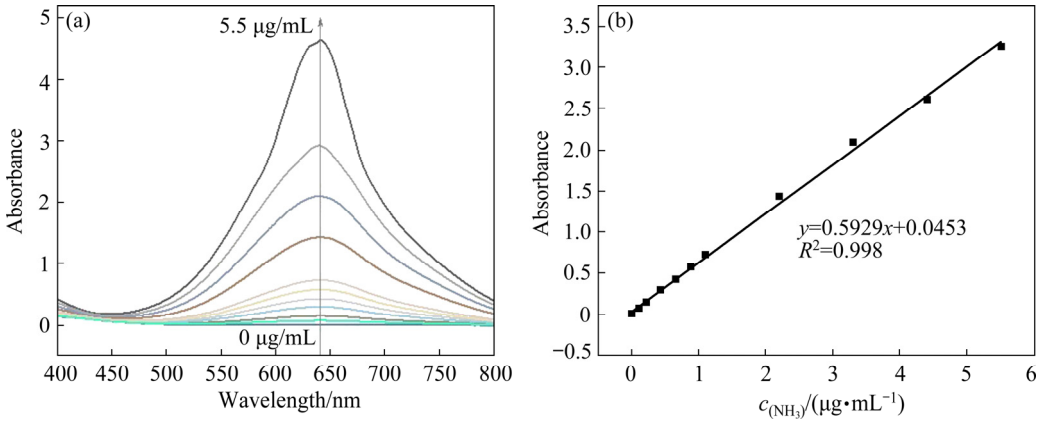

Fig. 6 UV-Vis absorption spectra of ammonia solutions after adding indophenol blue solution (a), and standard curve for NH_3 detection with indophenol blue method (b)

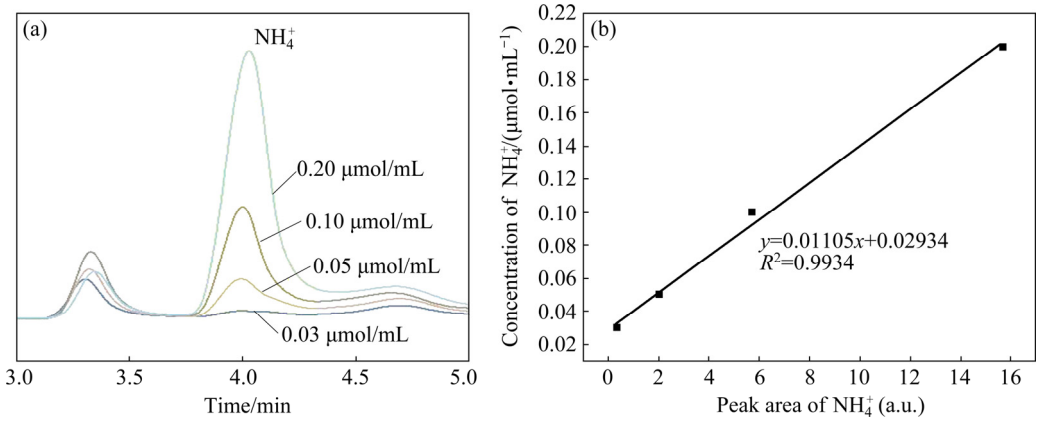

Fig. 7 Spectra of ion chromatography for NH_4Cl solution with different concentrations (a), and standard curve of NH_4Cl concentration vs peak area of NH_4^+ in ion chromatography spectra (b)

disperse the catalysts evenly in water, then bubbled with purified $^{14}N_2$ at a flow velocity of ~30 mL/min for 20 min. Subsequently, the suspension was agitated on a magnetic stirrer accompanied by irradiation of xenon lamp under full spectrum for 30 min. Before the ^{1}H-NMR measurement, we centrifugally separated the catalysts from the mixture, followed by adjusting the pH of the reaction solution to 2 with a few drops of hydrochloric acid. Then, the obtained solution was concentrated to about 20 μL and mixed with 0.6 mL d_6-DMSO to acquire ^{14}N labelled reactant solution. After that, the obtained ^{14}N labelled reactant solution was analyzed by ^{1}H-NMR spectroscopy (400 MHz). The concentration of $^{14}NH_4Cl$ was calculated according to the standard curve and the peak area of $^{14}NH_4Cl$ in ^{1}H-NMR spectra.

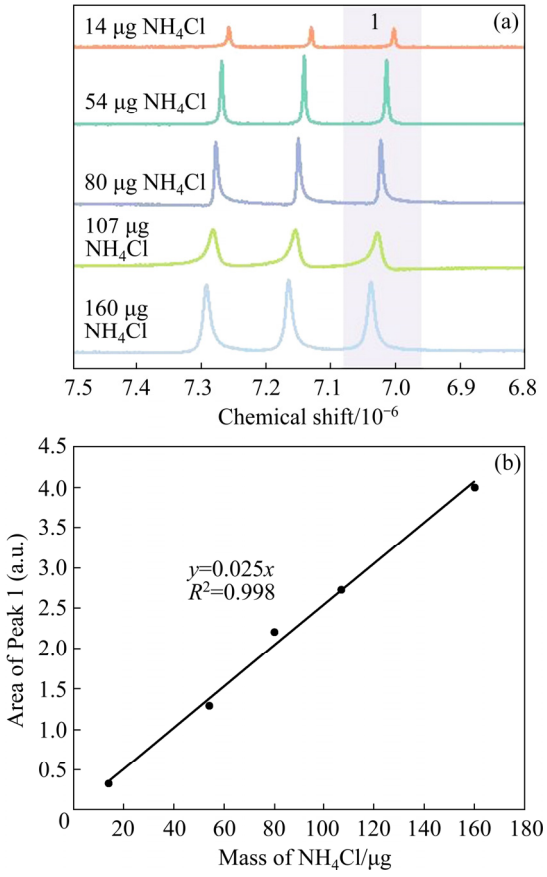

Fig. 8 ^{1}H-NMR (400 MHz) spectra of $^{14}NH_4Cl$ solution with different concentrations (a), and standard curve of mass of $^{14}NH_4Cl$ vs peak area of $^{14}NH_4Cl$ in ^{1}H-NMR (400 MHz) spectra (b)

2.11 ^{15}N isotope labelling experiments

For the verification of the N source of synthetic ammonia, we conducted ^{15}N isotope labeling experiments. In a typical ^{15}N isotope labeling experiment, 20 mL of ultrapure water and 10 mg of purified photocatalysts were added into the 100 mL glass reaction reactor. Subsequently, we charged and discharged the reaction reactor with 0.4 MPa of high-purity Ar, then pumped the reaction reactor to vacuum. Next, we charged 0.2 MPa of $^{15}N_2$ into the reaction bottle, rather than bubbled purified $^{15}N_2$ for 20 min due to the high cost of $^{15}N_2$. The remaining irradiation steps were the same as above photocatalytic reaction steps. After the reaction was over, the reaction solution was collected by suction filtration. We used hydrochloric acid to adjust the pH value of the filtrate to 2 and concentrated the solution to about 20 μL. Then, 0.6 mL of d6-DMSO was added into the solution and the obtained sample was measured by ^{1}H-NMR spectroscopy.

2.12 Detection of O_2

A FULI 9790 II-GC equipped with a thermal conductivity detector (TCD) was used for determination of O_2. For the calibration of standard relation curve of volume vs peak area, 10, 20, 30, 40, 50, 80, and 100 μL of O_2 were respectively injected to the gas chromatography (GC) using a gastight syringe (Hamilton, 1000 μL). We drew the profile of peak area vs the volume of O_2, where a linear correlation with R^2=0.9963 was acquired (Fig. 9). In order to estimate the generated O_2 during photocatalytic process, a 100 mL glass reactor equipped with gas sample was employed. In a typical reaction, 20 mL of ultrapure water and 10 mg of purified photocatalysts were added into the reactor. The mixture was sonicated for 5 min and then bubbled with purfied N_2 with a flow velocity of ~30 mL/min for 20 min. Subsequently, the reaction flask was sealed and left to stand in dark for 30 min. Before light irradiation, 0.2 mL of the gas was extracted from the reactor to determine the amount of residual O_2. After light irradiation, the gaseous products (0.2 mL) from the reactor were taken out at regular intervals for analysis.

2.13 Apparent quantum efficiency (AQE) measurements

The photocatalytic reaction used to determine AQE was counduted in a quartz top-radiation reactor. Diverse monochromatic LED lights centered on 490, 535, 595, 630 and 740 nm (Perfect

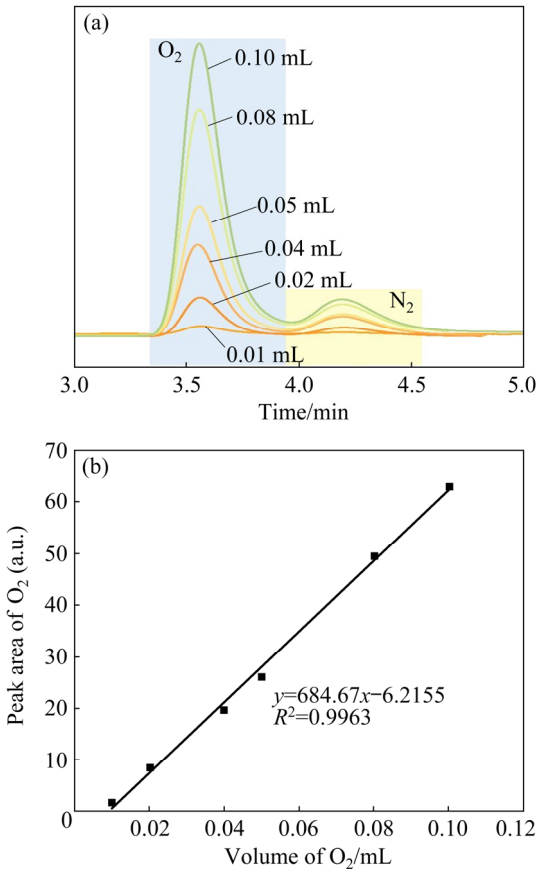

Fig. 9 Chromatograms of O_2 with different volumes (a), and plot of O_2 volume vs peak area (b)

light, PLS-LED100B) were used as the light source. The AQEs (η) under different monochromatic LED lights were calculated by

$$\eta=\frac{N_e}{N_p}=\frac{3N_{NH_3}}{N_p}=\frac{3n_{NH_3}N_A}{WAt/(hv)}\times 100\% \quad (1)$$

where N_{NH_3}, N_p and N_e represent numbers of the generated NH_3, the incident photons, and the reacted electrons, respectively; W, A and t represent the light intensity, irradiation area and time, respectively; v represents the light frequency; h is Planck constant; N_A is the Avogadro's constant.

2.14 Photoelectrochemical measurement

The initial ITO glass was cut into small pieces of 2 cm × 1.2 cm, then ultrasonically washed with acetone (30 min), ethanol (30 min) and H_2O (30 min), respectively. 10 mg of catalysts were added into 0.1 mL of ethanol, followed by sonication for 30 min to make the catalysts evenly dispersed. The as-obtained suspension liquid was dropwise added onto two pieces of 2 cm × 1.2 cm ITO glasses. Then, the obtained ITO glasses were dried under vacuum at 80 °C for 6 h. The photoelectrochemical experiments were conducted on a Squidstst Plus electrochemical station (Admiral Instruments) at RT by using standard three-electrode method. NaCl aqueous solution (0.5 mol/L) was used as the electrolyte. The working electrode, counter electrode and reference electrode are modified catalyst-coated ITO glass, a Pt foil and a Ag/AgCl electrode, respectively.

2.15 DFT calculations

All calculations were performed by using the plane wave density functional theory (DFT) code VASP [40]. The projector-augmented wave (PAW) [41] with the generalized gradient approximation (GGA) refined by Perdew, Burke and Ernzerhof (PBE) [42] was used as well. During geometry optimization, the convergence of energy and forces were set to be 1×10^{-5} eV and 0.02 eV/Å, respectively. The energy cutoff was set to be 450 eV. Spin unrestricted calculation was applied in all cases. A vacuum distance was set to be 15 Å in order to eliminate the interactions between layers and their neighboring layers. All structures were optimized by using a Monkhorst–Pack grid of 4 × 4 × 1, which have a=9.08 Å, b=9.08 Å. GGA+U method was used with U_{eff}=3 eV for Ti 3d orbitals. The substrates were cleaved with four layers and the bottom two layers were fixed. The Van der Waals interaction was calculated by the DFT-D3 method [43].

2.16 Instrumentations

The XRD patterns were collected by a Rigaku X-ray diffractometer (Rigaku, MiniFlex 600) with Cu K_α radiation (λ=1.54178 Å). The morphology was characterized by scanning electron microscopy (SEM, Quanta FEG 250). TEM and HAADF-STEM images were obtained on a field-emission transmission electron microscope (JEOL, ARM−200F) which was operated at an acceleration voltage of 200 kV. Electron spin resonance (ESR) spectra were carried out on an ESR spectrometer (JEOL, JES-FA200) at 298 K. X-ray photoemission spectroscopy (XPS) experiments were implemented at BL10B beamline in the National Synchrotron Radiation Laboratory (NSRL) in Hefei, China. The UV−Vis absorption experiments were carried out on a double beam UV-Vis spectrophotometer

(Persee, TU−1901). The temperature-programmed desorption of N_2 (N_2-TPD) tests were conducted on temperature programmed adsorption analyzer (Vodo, VDsorb−91i). Elimination of NO_x in raw gas was conducted on a fixed bed reactor (Vodo, VDRT−200SMT). ^{1}H-NMR spectroscopy was collected on a 400M Nuclear Magnetic Resonance spectroscopy (AVANCEIII 400M). NH_4^+ cation was decected by the ion chromatograph (SHINE, CIC-D120). The inductively coupled plasma optical emission spectrometry (ICP-OES) experiments were implemented on a plasma spectrometer (SPECTRO, SPECTRO BLUE SOP).

3 Results and discussion

3.1 Characterization of photocatalysts

At the beginning, Ti_3AlC_2 powder was synthesized by ball milling of TiC, TiH_2, and Al precursor powders followed by calcination and grinding [35]. W/Ti_3AlC_2 powder was prepared by the procedure similar to that for Ti_3AlC_2 powder, except adding W powder in the ball milling process as well as reducing the amount of TiH_2 powder (Fig. 10(a)). Further selectively etching Al layers from Ti_3AlC_2 and W/Ti_3AlC_2 powders by HF at RT for 20 h, $Ti_3C_2T_x$-NU and W/$Ti_3C_2T_x$-NU MXenes with the accordion-like morphology were obtained (Figs. 10(b, c)). After the treatment of $Ti_3C_2T_x$-NU and W/$Ti_3C_2T_x$-NU MXenes with DMSO and ultrasonication insequence, two-dimension materials of $Ti_3C_2T_x$-U and W/$Ti_3C_2T_x$-U MXenes were prepared (see Figs. 10(d, e)). The nanosheet morphology of W/$Ti_3C_2T_x$-U was well characterized by the HAADF-STEM as displayed in Figs. 10(f) and (g). Figure 10(g) exhibited a magnified HAADF-STEM of W/$Ti_3C_2T_x$-U. Isolated W atoms, which were observed as bright spots, were uniformly dispersed in W/$Ti_3C_2T_x$-U MXene. In addition, a scheme of atomic columns was depicted

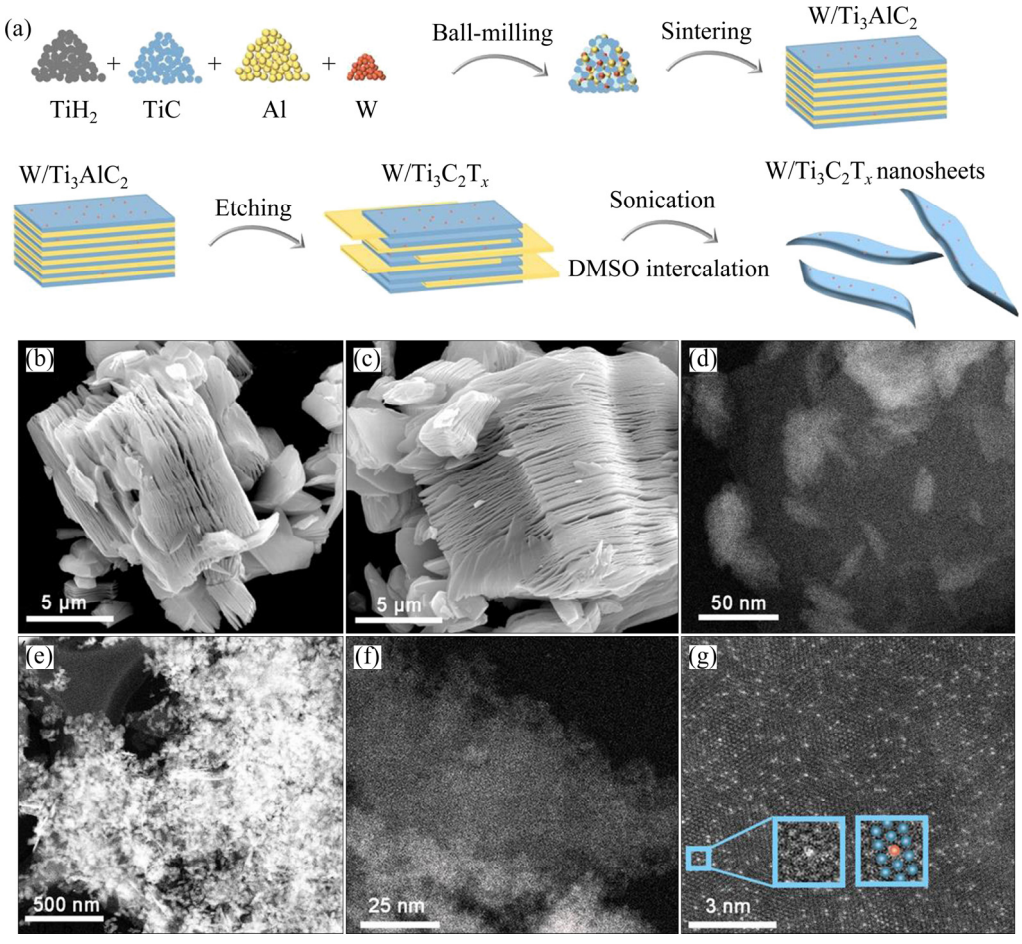

Fig. 10 Schematic illustration of synthetic procedure for W/$Ti_3C_2T_x$-U (a), SEM images of $Ti_3C_2T_x$-NU (b) and W/$Ti_3C_2T_x$-NU (c), HAADF-STEM images of $Ti_3C_2T_x$-U (d) and W/$Ti_3C_2T_x$-U (e, f), and magnified HAADF-STEM image of W/$Ti_3C_2T_x$-U (g) (Schematic columns of atoms are overlaid on the magnified experimental image (inset image in (g))

by directly overlaying on the experimental HAADF-STEM image for better comparison (inset image in Fig. 10(g)). The orange dot of W atom was exactly located at the lattice plane walls of the blue columns of Ti atoms rather than in the spacings between them. As such, the isolated W atoms were stabilized in the Ti vacancies by substitution, consistent with the synthetic procedures by slightly decreasing the amount of TiH_2 for W/Ti_3AlC_2 powder. Furthermore, the metallic molar fractions of W element in $W/Ti_3C_2T_x$-NU and $W/Ti_3C_2T_x$-U MXenes were determined as 2.0% and 1.9% by ICP-OES, respectively. Based on the above results, we successfully doped W atoms into $Ti_3C_2T_x$ MXenes by facilely adjusting the molar ratio of W to TiH_2 in precursor powders. More importantly, the simplicity of this doping procedure allowed us to prepare catalysts in large scale, where up to 1.39 g of $W/Ti_3C_2T_x$-U MXenes was prepared in one procedure.

We further explored the electronic properties of as-obtained samples in detail. Figure 11(a) showed the O 1s XPS spectra, four peaks could be fitted into surface adsorbed oxygen species (O*) at 533.1 eV, OH groups at 532.0 eV, oxygen vacancies (OVs) at 531.0 eV and the surface oxygen atoms bonded to titanium atoms (denoted as surface O—Ti species) at 529.7 eV, respectively [44,45]. Apparently, the O 1s spectrum of $Ti_3C_2T_x$-NU was quite similar to that of $W/Ti_3C_2T_x$-NU. As for $Ti_3C_2T_x$-U and $W/Ti_3C_2T_x$-U, the peaks for surface O—Ti species and OVs were significantly strengthened. The presence of OVs was further proved by ESR spectroscopy. As shown in Fig. 11(b), $Ti_3C_2T_x$-U and $W/Ti_3C_2T_x$-U revealed strong features with g value of 2.001, which was assigned to the OVs occupied by electrons [46]. No such signal attributed to OVs was detected for $Ti_3C_2T_x$-NU and $W/Ti_3C_2T_x$-NU.

Figure 12(a) showed the XPS spectra of Ti 2p, which was fitted into three major components including Ti—C at 460.8 and 455.0 eV, Ti—O at 464.4 and 458.5 eV, and Ti−F at 461.9 and 457.8 eV, respectively [44,47]. Apparently, peaks of Ti—O for $Ti_3C_2T_x$-U and $W/Ti_3C_2T_x$-U were significantly strengthened relative to these for $Ti_3C_2T_x$-NU and $W/Ti_3C_2T_x$-NU. The C 1s XPS spectra of as-obtained samples are displayed in Fig. 12(b). The peaks located at 280.6 and 281.2 eV are assigned to C 1s of Ti—C bond on the surface of

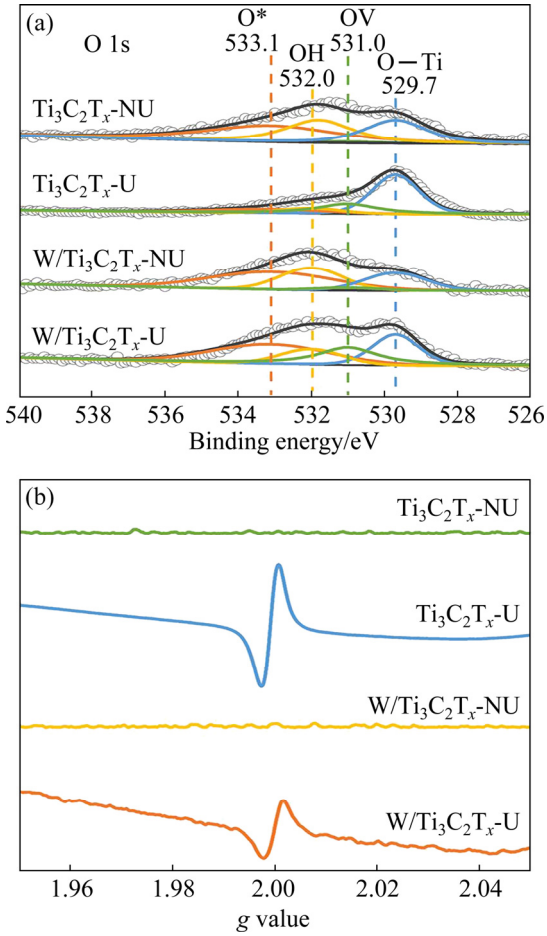

Fig. 11 O 1s XPS spectra (a) and ESR signals (b) of $Ti_3C_2T_x$-NU, $Ti_3C_2T_x$-U, $W/Ti_3C_2T_x$-NU, and $W/Ti_3C_2T_x$-U

the prepared samples. The peaks at 284.6 and 288.3 eV are attributed to C═C and C—Ti—O bond, respectively [48,49]. Compared with $Ti_3C_2T_x$-NU and $W/Ti_3C_2T_x$-NU, the Ti—C bonds of $Ti_3C_2T_x$-U and $W/Ti_3C_2T_x$-U showed a clear negative shift in binding energy of about 0.6 eV. Meanwhile, the peaks for Ti — C — O were significantly strengthened, which indicated the formation of $Ti_3C_2O_x$ moieties after the intercalation and ultrasonic treatment. As for the XPS spectra of W 4f, the signal of both $W/Ti_3C_2T_x$-NU and $W/Ti_3C_2T_x$-U could be fitted into W^{6+}, W^{4+}, and $W^{\delta+}$ species (Fig. 12(c)) [50,51]. Thus, W atoms in $W/Ti_3C_2T_x$-NU and $W/Ti_3C_2T_x$-U were mainly in the oxidized state.

3.2 Catalytic performance in N_2 photofixation

For the estimation of catalytic performances of the obtained catalysts towards N_2 photofixation, the generated NH_3 was measured by spectrophotometry

with Nessler's regent. A blank test was conducted with merely N_2 saturated ultrapure water under the irradiation of Xenon lamp, no NH_3 was detected. In addition, no product was observed without light irradiation, replacing H_2O with CH_3CN or replacing N_2 with Ar (Table 1).

Figure 13(a) illustrated the NH_3 production rate over $Ti_3C_2T_x$-NU, $Ti_3C_2T_x$-U, $W/Ti_3C_2T_x$-NU, and $W/Ti_3C_2T_x$-U catalysts under full spectrum irradiation. The NH_3 production rates were 8.9, 14.5, and 64.4 μmol/(g·h) for $Ti_3C_2T_x$-NU, $Ti_3C_2T_x$-U, and $W/Ti_3C_2T_x$-NU, respectively. When the reaction was catalyzed by $W/Ti_3C_2T_x$-U, the NH_3 production rate reached 227.5 μmol/(g·h). The excellent catalytic performance of $W/Ti_3C_2T_x$-U was rechecked by the combination of ion chromatography, indophenol blue colorimetry and ^1H NMR. The comparable result confirmed the reliability of the ammonia detection by Nessler's reagent colorimetry (Table 2 and Fig. 13(b)).

The origin of NH_3 was further verified by ^{15}N isotope labeling experiment. As shown in Fig. 3(b), the doublets of $^{15}NH_4^+$ were clearly observed for isotopic labelled sample, indicating that the $^{15}N_2$ served as the N source of synthetic ammonia. We further investigated the catalytic performance of $W/Ti_3C_2T_x$-U under monochromatic light with different wavelengths. $W/Ti_3C_2T_x$-U exhibited favorable activity for N_2 photocatalytic fixation in the full-spectrum region of sunlight (Fig. 13(c)). NH_3 production rate of 43.6 μmol/(g·h) was still achieved by $W/Ti_3C_2T_x$-U after being irradiated by monochromatic LED lights centered at 630 nm. When we changed the light source to monochromatic LED lights centered at 740 nm, the NH_3 production rate of $W/Ti_3C_2T_x$-U achieved 28.0 μmol/(g·h). For the evaluation of light utilization efficiency of $W/Ti_3C_2T_x$-U, we conducted the wavelength-dependent AQE tests by measuring the amount of generated NH_3 (Fig. 13(d)). Specifically, the AQEs of $W/Ti_3C_2T_x$-U were 0.05%−0.15% in UV-Vis and NIR wavelengths. More importantly, we explored the stability of $W/Ti_3C_2T_x$-U by analyzing the catalytic performance over successive rounds of reaction (Fig. 13(e)). $W/Ti_3C_2T_x$-U was able to maintain catalytic activity >90% for ten rounds of reaction. We also performed long-term test for $W/Ti_3C_2T_x$-U,

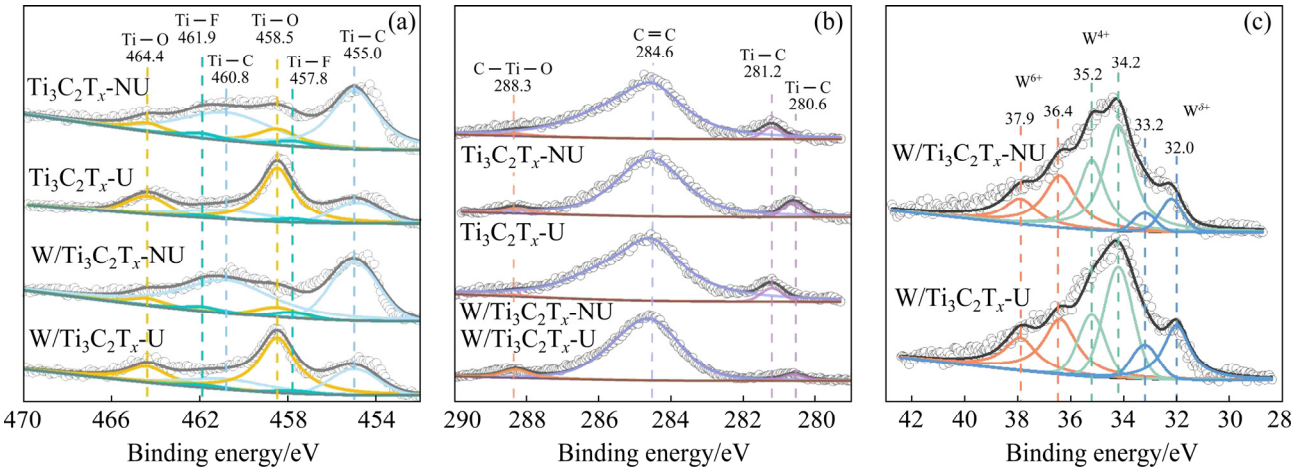

Fig. 12 Ti 2p (a) and C 1s (b) XPS spectra of $Ti_3C_2T_x$-NU, $Ti_3C_2T_x$-U, $W/Ti_3C_2T_x$-NU and $W/Ti_3C_2T_x$-U, and W 4f XPS spectra of $W/Ti_3C_2T_x$-NU and $W/Ti_3C_2T_x$-U (c)

Table 1 Photocatalytic N_2 fixation over $W/Ti_3C_2T_x$-U under various reaction conditions[a)]

Calalyst	Atmosphere	Solvent	Light	NH_3 production
No	N_2	H_2O	Full-spectrum	N.D.[b)]
$W/Ti_3C_2T_x$-U	N_2	H_2O	Without light	N.D.[b)]
$W/Ti_3C_2T_x$-U	N_2	CH_3CN	Full-spectrum	N.D.[b)]
$W/Ti_3C_2T_x$-U	Ar	H_2O	Full-spectrum	N.D.[b)]

[a)] Reaction condition: catalyst 10 mg, light intensity 250 mW/cm^2, solvent 20 mL, reaction time 0.5 h, and ^1H-NMR method was used to quantify the generated NH_3; [b)] N.D. represents not detected

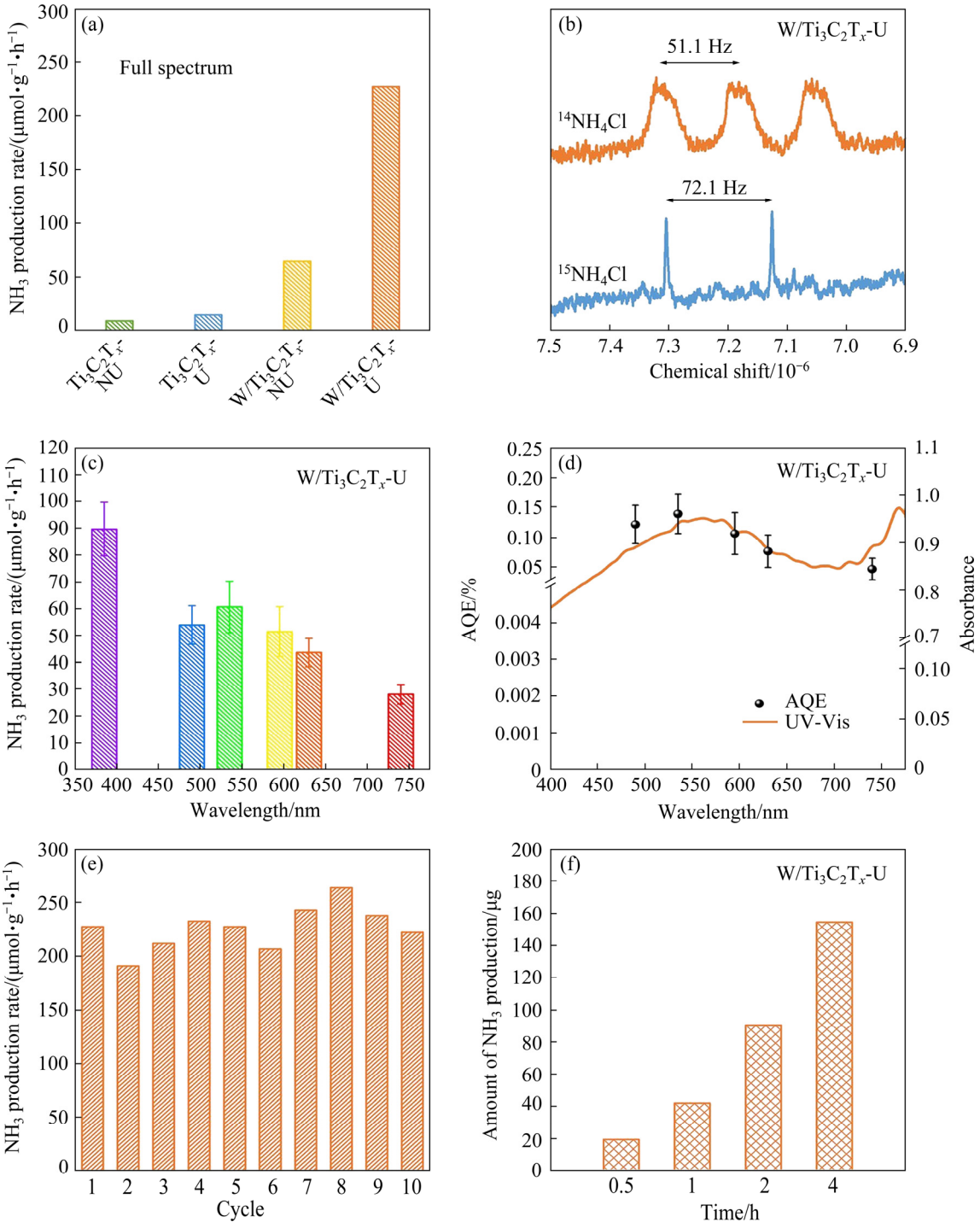

Fig. 13 NH_3 production rates over $Ti_3C_2T_x$-NU, $Ti_3C_2T_x$-U, W/$Ti_3C_2T_x$-NU and W/$Ti_3C_2T_x$-U, under irradiation of full spectrum (a), ^{1}H-NMR (400 MHz) spectra of solution after photocatalytic N_2 fixation by using W/$Ti_3C_2T_x$-U as photocatalyst in $^{14}N_2$ and $^{15}N_2$ atmosphere (b), photocatalytic NH_3 production rates over W/$Ti_3C_2T_x$-U under monochromatic light irradiation (c), calculated AQEs for N_2 fixation over W/$Ti_3C_2T_x$-U under monochromatic light irradiation (d), NH_3 production rates of W/$Ti_3C_2T_x$-U over course of ten rounds of successive reaction (e), and amount of generated NH_3 over W/$Ti_3C_2T_x$-U at different time intervals under irradiation of full spectrum (f)

where NH_3 gradually generated by prolonging reaction time and up to 154.5 μmol NH_3 was produced after 4 h (Fig. 13(f)). In addition, the generated O_2 during N_2 photofixation was also measured over W/$Ti_3C_2T_x$-U. The generation of NH_3 was accompanied with the production of O_2, proving that N_2 reduction by hot electrons coupling the oxidation of water by hot holes (Fig. 14).

Table 2 Calculated ammonia production rates based on different detection methods during N_2 photofixation over $W/Ti_3C_2T_x$-U

Detection method	NH_3 production rate/ ($\mu mol \cdot g^{-1} \cdot h^{-1}$)
Nessler's reagent	227.5
Indophenol blue	265.3
Ion chromatograph	227.5
^{1}H-NMR (400 MHz)	201.5

3.3 Role of W atom and $Ti_3C_2T_x$-U

To investigate the causes of superior N_2 photocatalytic reduction performance of $W/Ti_3C_2T_x$-U, we conducted the UV-Vis, photoelectrochemical, and N_2 TPD experiments to research the property of obtained catalysts. As shown in diffuse reflectance UV-Vis spectra of obtained samples (Fig. 15(a)), $Ti_3C_2T_x$-NU and $Ti_3C_2T_x$-U exhibited absorption of both the UV-Vis and NIR range of 300−770 nm. After doping by W atoms, $W/Ti_3C_2T_x$-NU and $W/Ti_3C_2T_x$-U showed even stronger absorption ability at ~550 and ~720 nm relative to that for $Ti_3C_2T_x$-NU and $Ti_3C_2T_x$-U. Estimated by Kubelka−Munk function, the band gaps of $Ti_3C_2T_x$-NU, $Ti_3C_2T_x$-U, $W/Ti_3C_2T_x$-NU and $W/Ti_3C_2T_x$-U were 1.32, 1.37, 1.40 and 1.44 eV, respectively. It showed that both W atom doping and ultrasonic intercalation result in an increase in

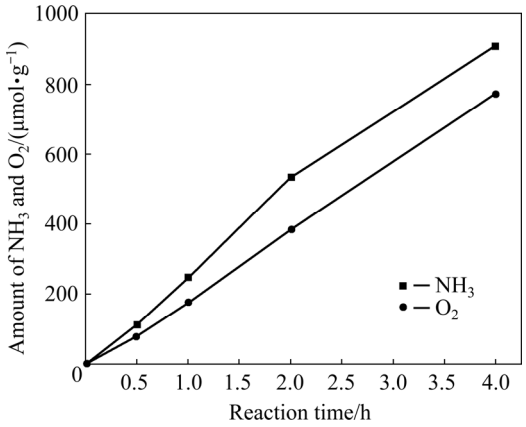

Fig. 14 Photocatalytic production of NH_3 and O_2 during N_2 fixation over $W/Ti_3C_2T_x$-U in pure water without any sacrificial agents in sealed reactor

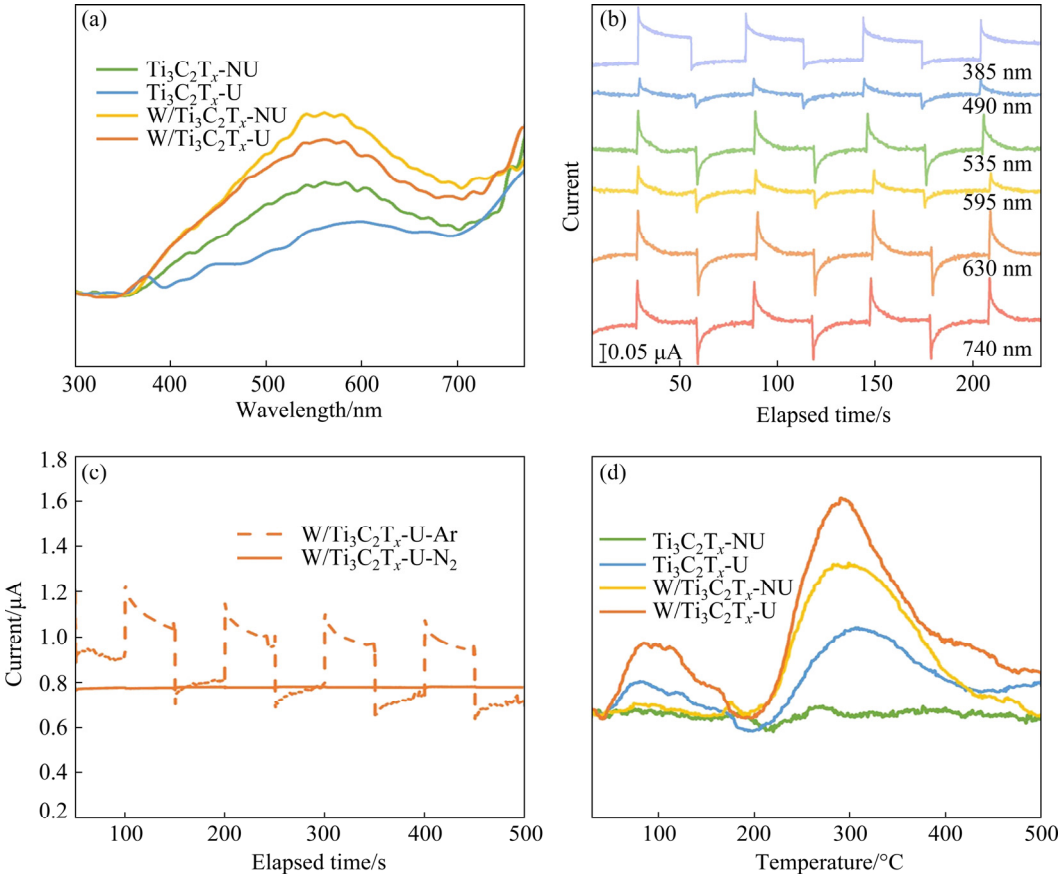

Fig. 15 Diffuse reflectance UV–Vis spectra of $Ti_3C_2T_x$-NU, $Ti_3C_2T_x$-U, $W/Ti_3C_2T_x$-NU and $W/Ti_3C_2T_x$-U (a), photocurrent responses of $W/Ti_3C_2T_x$-U under monochromatic light irradiation in Ar atmosphere (b), photocurrent responses of $W/Ti_3C_2T_x$-U under full-spectrum irradiation (320−780 nm) of xenon lamp (250 mW/cm^2) with Ar/N_2 atomosphere (c), and N_2-TPD profiles of $Ti_3C_2T_x$-NU, $Ti_3C_2T_x$-U, $W/Ti_3C_2T_x$-NU and $W/Ti_3C_2T_x$-U (d)

band gap of ~0.05 eV. In addition, the photo-electrochemical method further verified the response of W/$Ti_3C_2T_x$-U to UV-Vis and NIR monochromatic light by the transient photocurrent responses under Ar atmosphere. An obvious photocurrent response appeared under the illumination of monolights across 385−740 nm in Fig. 15(b). When we changed N_2 atmosphere to saturate the electrolyte, the transient photocurrent responses under the irradiation of xenon lamp significantly decreased, indicating the transfer of photogenerated electrons to chemisorb N_2 molecules (Fig. 15(c)). Besides, N_2 TPD was also applied to investigating the adsorption properties of N_2 on the catalysts (Fig. 15(d)). The peak at ~100 °C was originated from the physical absorption of N_2, while the peak centered at 300 °C was attributed to chemisorbed N_2 [9]. W/$Ti_3C_2T_x$-NU and W/$Ti_3C_2T_x$-U exhibited stronger peaks for chemisorption of N_2 than $Ti_3C_2T_x$-U, while $Ti_3C_2T_x$-NU exhibited nearly no peaks in N_2 TPD profile. Accordingly, doped W atoms acted as the active sites to promote the adsorption of N_2 molecules. Moreover, the OVs generated on $Ti_3C_2T_x$-U and W/$Ti_3C_2T_x$-U also provided synergistic sites for promoting both physical and chemical adsorption of N_2.

Furthermore, we also provided atomic-level insights into the reaction pathways by theoretical calculations. The DFT studies were conducted with two models of $Ti_3C_2O_2$ — V with an OV and W/$Ti_3C_2O_2$ — V with an OV. The calculated N_2 adsorption energies on $Ti_3C_2O_2$ — V and W/$Ti_3C_2O_2$—V were −0.37 and −0.38 eV, respectively. In addition, the electron density of adsorbed N_2 was also calculated. The adsorbed N_2 accepted 0.34e from W/$Ti_3C_2O_2$—V, while $Ti_3C_2O_2$—V donated only 0.05e to adsorb N_2 (Figs. 16(a)−(d)). The transformation of electrons to adsorb N_2 would fill the anti-bonding orbital, resulting in the weakening of N≡N with the elongation of bond length. Thus, doped-W atoms directly promoted the adsorption and activation of N_2 molecules. Moreover, the possible intermediates and optimal reaction paths over $Ti_3C_2O_2$—V (Fig. 16(e)) and W/$Ti_3C_2O_2$—V (Fig. 16(f)) were screened. The reduction of N_2 to NH_3 over $Ti_3C_2O_2$—V was apt to the distal pathway where the transformation of N_2* to N_2H* species as

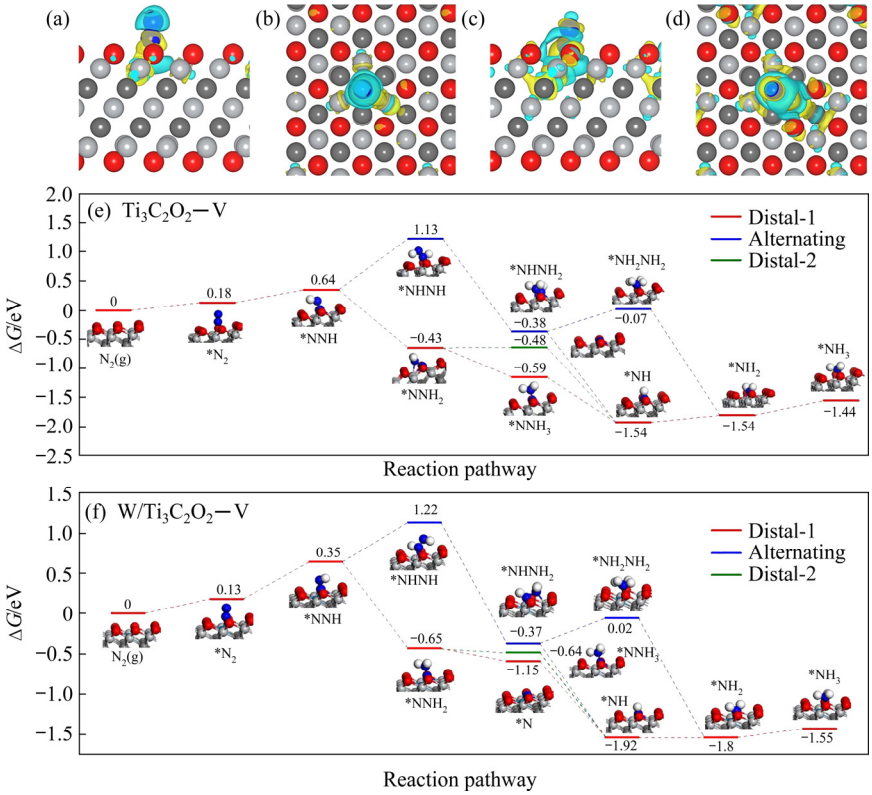

Fig. 16 Side view (a, c) and top view (b, d) of electron density diagrams of adsorbed N_2 on model of $Ti_3C_2O_2$—V (a, b) and W/$Ti_3C_2O_2$—V (c, d), alternate pathway and distal pathway for dissociation of N_2 to NH_3 over $Ti_3C_2O_2$—V (e) and W/$Ti_3C_2O_2$—V (f) (* represents the adsorbed sites. The brick red, grey, dark grey, blue, dark blue and white balls represent O, Ti, C, W, N and H atoms, respectively)

the rate-limiting step. The reaction energy (ΔG) of this transformation was 0.46 eV for $Ti_3C_2O_2$—V. When it comes to W/$Ti_3C_2O_2$ — V, the distal pathway is also the optimal reaction channel towards N_2 fixation. The value of ΔG for the step of N_2* to N_2H* species was as low as 0.22 eV over W/$Ti_3C_2O_2$—V. In addition, the hydrogenation of NH_2* to NH_3* species was the bottleneck over W/$Ti_3C_2O_2$—V, with the ΔG value of this step to be 0.25 eV. Hence, doped-W atoms worked as active centers to play an effective role in adsorbing, activating and transferring N_2 molecules. In addition, MXenes were able to harvest sunlight across UV-Vis to NIR regions. As a result, W/$Ti_3C_2T_x$-U realized full-spectrum photofixation of N_2 by integration of unique optical properties and highly active sites.

4 Conclusions

(1) W/$Ti_3C_2T_x$-U realized full-spectrum photofixation of N_2 by integration of unique optical properties of $Ti_3C_2T_x$ MXenes and highly active W sites. High NH_3 production rate of 228 μmol/(g·h) was achieved over W/$Ti_3C_2T_x$-U under the irradiation of xenon lamp at RT without sacrificial agents.

(2) $Ti_3C_2T_x$ MXene harvests UV-Vis and NIR light to generate hot electrons. In addition, after ultrasonic intercalation, the accordion-like $Ti_3C_2T_x$ MXene ($Ti_3C_2T_x$-NU) was transformed to $Ti_3C_2T_x$ MXene nanosheets ($Ti_3C_2T_x$-U) with more surface —O terminations and OVs.

(3) Doped-W atoms work as the active sites to promote the physical and chemical adsorption of N_2, and lower reaction energy in N_2 reduction by donating electrons to the anti-bonding orbital of N_2 molecules to elongate the bond length of N≡N.

Acknowledgments

This work was supported by the National Natural Science Foundation of China (Nos. 51801235, 11875258, 11505187, 51374255, 51802356, 51572299, 41701359), and the Natural Science Foundation of Hunan Province, China (No. 2020JJ5690).

References

[1] YU Xiao-min, HAN Peng, WEI Zeng-xi, HUANG Lin-song, GU Zheng-xi, PENG Si-jia, MA Jian-min, ZHENG Geng-feng. Boron-doped graphene for electrocatalytic N_2 Reduction [J]. Joule, 2018, 2: 1610−1622.

[2] PFROMM P H. Towards sustainable agriculture: Fossil-free ammonia [J]. Journal of Renewable and Sustainable Energy, 2017, 9: 034702.

[3] ZHAO Yu-fei, ZHAO Yuan-xuan, WATERHOUSE G I N, ZHENG Li-rong, CAO Xing-zong, TENG Fei, WU Li-zu, TUNG C H, O'HARE D, ZHANG Tie-rui. Layered-double-hydroxide nanosheets as efficient visible-light-driven photocatalysts for dinitrogen fixation [J]. Advanced Materials, 2017, 29: 1703828.

[4] HOU Ting-ting, PENG Hai-long, XIN Yue, WANG San-mei, ZHU Wen-kun, CHEN Lan-lan, YAO Yuan, ZHANG Wen-hua, LIANG Shu-quan, WANG Liang-bing. Fe single-atom catalyst for visible-light-driven photofixation of nitrogen sensitized by triphenylphosphine and sodium iodide [J]. ACS Catalysis, 2020, 10: 5502−5510.

[5] XU Chen-min, QIU Peng-xiang, LI Li-yuan, CHEN Huan, JIANG Fang, WANG Xin. Bismuth subcarbonate with designer defects for broad-spectrum photocatalytic nitrogen fixation [J]. ACS Applied Materials & Interfaces, 2018, 10(30): 25321−25328.

[6] HU Can-yu, CHEN Xing, JIN Jian-bo, HAN Yong, CHEN Shuang-ming, JU Huan-xin, CAI Jun, QIU Yun-rui, GAO Chao, WANG Chen-ming, QI Ze-ming, LONG Ran, SONG Li, LIU Zhi, XIONG Yu-jie. Surface plasmon enabling nitrogen fixation in pure water through a dissociative mechanism under mild conditions [J]. Journal of the American Chemical Society, 2019, 141: 7807−7814.

[7] ZHANG Shuai, ZHAO Yun-xuan, SHI Run, ZHOU Chao, WATERHOUSE G I N, WU Li-zhu, TUNG Chen-ho, ZHANG Tie-rui. Efficient photocatalytic nitrogen fixation over $Cu^{\delta+}$-modified defective ZnAl-layered double hydroxide nanosheets [J]. Advanced Energy Materials, 2020, 10: 1901973.

[8] ZHAO Yun-xuan, ZHENG Li-rong, SHI Run, ZHANG Shuai, BIAN Xuan-ang, WU Fan, CAO Xing-zhong, WATERHOUSE G I N, ZHANG Tie-rui. Alkali etching of layered double hydroxide nanosheets for enhanced photocatalytic N_2 reduction to NH_3 [J]. Advanced Energy Materials, 2020, 10: 1901973.

[9] GAO Xiang, AN Li, QU Dan, JIANG Wen-shuai, CHAI Yan-xiao, SUN Shao-rui, LIU Xing-yuan, SUN Zai-cheng. Enhanced photocatalytic N_2 fixation by promoting N_2 adsorption with a co-catalyst [J]. Science Bulletin, 2019, 64: 918−925.

[10] QIAN Jing, ZHAO Sen, DANG Wen-qiang, LIAO Yuan, ZHANG Wen, WANG Hui, LV Ling-ling, LUO Lei, JIANG Hai-ying, TANG Jun-wang. Photocatalytic nitrogen reduction by Ti_3C_2 MXene derived oxygen vacancy-rich C/TiO_2 [J]. Advanced Sustainable Systems, 2021, 5: 2000282.

[11] HAO Chong-yan, LIAO Yuan, WU Yang, AN Ya-jing, LIN Jian-nan, GU Zheng-fei, JIANG Min-hong, HU Shi, WANG Xiao-tian. RuO_2-loaded TiO_2–MXene as a high performance photocatalyst for nitrogen fixation [J]. Journal of Physics and Chemistry of Solids, 2020, 136: 109141.

[12] GUO Chun-xian, RAN Jing-run, VASILEFF A, QIAO Shi-Zhang. Rational design of electrocatalysts and photo(electro) catalysts for nitrogen reduction to ammonia

(NH_3) under ambient conditions [J]. Energy & Environmental Science, 2018, 11: 45−56.

[13] ZHAO Yun-xuan, ZHAO Yu-fei, SHI Run, WANG Bin, WATERHOUSE G I, WU Li-zhu, TUNG Chen-ho, ZHANG Tie-rui. Tuning oxygen vacancies in ultrathin TiO_2 nanosheets to boost photocatalytic nitrogen fixation up to 700 nm [J]. Advanced materials, 2019, 31: 1806482.

[14] YAN Jun-qing, WANG Tuo, WU Guang-jun, DAI Wei-li, GUAN Nai-jia, LI Lan-dong, GONG Jin-long. Tungsten oxide single crystal nanosheets for enhanced multichannel solar light harvesting [J]. Advanced Materials, 2015, 27: 1580−1586.

[15] YANG Yong-qiang, YIN Li-chang, GONG Yue, NIU Ping, WANG Jian-qiang, GU Lin, CHEN Xing-qiu, LIU Gang, WANG Lian-zhou, CHENG Hui-ming. An unusual strong visible-light absorption band in red anatase TiO_2 photo-catalyst induced by atomic hydrogen-occupied oxygen vacancies [J]. Advanced Materials, 2018, 30: 1704479.

[16] MAY J W, MA J, BADAEVA E, LI X. Effect of excited-state structural relaxation on midgap excitations in Co^{2+}-doped ZnO quantum dots [J]. Journal of Physical Chemistry C, 2014, 118: 13152−13156.

[17] LIANG Liang, LI Xiao-dong, SUN Yong-fu, TAN Yuan-long, JIAO Xing-chen, JU Huan-xin, QI Ze-ming, ZHU Jun-fa, XIE Yi. Infrared light-driven CO_2 overall splitting at room temperature [J]. Joule, 2018, 2 (5): 1004−1016.

[18] HAN Yu, WU Ze-fei, XU Shui-gang, CHEN Xiao-long, WANG Lin, WANG Yang, XIONG Wei, HAN Tian-yi, YE Wei-guang, LIN Jiang-xia-zi, CAI Yuan, HO K M, HE Yu-heng, SU Dang-sheng, WANG Ning. Probing defect-induced midgap states in MoS_2 through graphene−MoS_2 heterostructures [J]. Advanced Materials Interfaces, 2015, 2: 1500064.

[19] BAI Song, ZHANG Ning, GAO Chao, XIONG Yu-jie. Defect engineering in photocatalytic materials [J]. Nano Energy, 2018, 53: 296−336.

[20] ZHANG Hua-bin, WANG Tao, WANG Jun-jie, LIU Hui-min, DAO T D, LI Mu, LIU Gui-gao, MENG Xian-guang, CHANG Kun, SHI Li, NAGAO T, YE Jin-hua. Surface-plasmon-enhanced photodriven CO_2 reduction catalyzed by metal-organic-framework-derived iron nanoparticles encapsulated by ultrathin carbon layers [J]. Advanced Materials, 2016, 28: 3703−3710.

[21] LI Cheng-cheng, WANG Tuo, ZHAO Zhi-jian, YANG Wei-min, LI Jian-feng, LI Ang, YANG Zhi-lin, OZIN G A, GONG Jin-long. Promoted fixation of molecular nitrogen with surface oxygen vacancies on plasmon-enhanced TiO_2 Photoelectrodes [J]. Angewandte Chemie-International Edition, 2018, 57: 5278−5282.

[22] ALI M, ZHOU Feng-ling, CHEN Kun, KOTZUR C, XIAO Chang-long, BOURGEOIS L, ZHANG Xin-yi, MACFARLANE D R. Nanostructured photoelectrochemical solar cell for nitrogen reduction using plasmon-enhanced black silicon [J]. Nature Communications, 2016, 7 11335.

[23] HOU Ting-ting, GUO Rui-han, CHEN Lan-lan, XIE Yang-ceng-zi, GUO Jia-sheng, ZHANG Wen-hua, ZHENG Xu-sheng, ZHU Wen-kun, TAN Xiao-ping, WANG Liang-bing. Atomic-level insights in tuning defective structures for nitrogen photofixation over amorphous SmOCl nanosheets [J]. Nano Energy, 2019, 65: 104003.

[24] YANG Ai-ling, LI Shun-pin, WANG Yu-jin, WANG Le-le, BAO Xi-chang, YANG Ren-qiang. Fabrication of Cu_2O@Cu_2O core–shell nanoparticles and conversion to Cu_2O@Cu core–shell nanoparticles in solution [J]. Transactions of Nonferrous Metals Society of China, 2015, 25: 3643−3650.

[25] YANG Jian-hua, GUO Yan-zhen, JIANG Rui-bin, QIN Feng, ZHANG Han, LU Wen-zheng, WANG Jian-fang, YU J C. High-efficiency “working-in-tandem” nitrogen photofixation achieved by assembling plasmonic gold nanocrystals on ultrathin titania nanosheets [J]. Journal of the American Chemical Society, 2018, 140: 8497−8508.

[26] DUCHENE J S, TAGLIABUE G, WELCH A J, CHENG W H, ATWATER H A. Hot hole collection and photoelectrochemical CO_2 reduction with plasmonic Au/p-GaN photocathodes [J]. Nano Letters, 2018, 18: 2545−2550.

[27] WEN Yan-yuan, DING Han-ming, SHAN Yong-kui. Preparation and visible light photocatalytic activity of Ag/TiO_2/graphene nanocomposite [J]. Nanoscale, 2011, 3: 4411−4417.

[28] LIM K R G, HANDOKO A D, NEMANI S K, WYATT B, JIANG Hai-ying, TANG Jun-wang, ANASORI B, SEH Z W. Rational design of two-dimensional transition metal carbide/nitride (MXene) hybrids and nanocomposites for catalytic energy storage and conversion [J]. ACS Nano, 2020, 14: 10834−10864.

[29] VELUSAMY D, EL-DEMELLAWI J, EL-ZOHRY A, GIUGNI A, LOPATIN S, HEDHILI M, MANSOUR A, DI FABRIZIO E, MOHAMMED O, ALSHAREEF H. MXenes for plasmonic photodetection [J]. Advanced Materials, 2019, 31: 1807658.

[30] SARYCHEVA A, MAKARYAN T, MALESKI K, ELUMALAI S, MELIKYAN A, MINASSIAN H, YOSHIMURA M, GOGOTSI Y. Two-dimensional titanium carbide (MXene) as surface-enhanced raman scattering substrate [J]. The Journal of Physical Chemistry C, 2017, 121: 19983−19988.

[31] CHAUDHURI K, ALHABEB M, WANG Z, SHALAEV V, GOGOTSI Y, BOLTASSEVA A. Highly broadband absorber using plasmonic titanium carbide (MXene) [J]. ACS Photonics, 2018, 5: 1115−1122.

[32] EL-DEMELLAWI J K, LOPATIN S, YIN J, MOHAMMED O F, ALSHAREEF H N. Tunable multipolar surface plasmons in 2D $Ti_3C_2T_x$ MXene flakes [J]. ACS Nano, 2018, 12: 8485−8493.

[33] MAUCHAMP V, BUGNET M, BELLIDO E P, BOTTON G A, MOREAU P, MAGNE D, NAGUIB M, CABIOC'H T, BARSOUM M W. Enhanced and tunable surface plasmons in two-dimensional Ti_3C_2 stacks: Electronic structure versus boundary effects [J]. Physical Review B, 2014, 89: 235428.

[34] ROEMER F M, WIEDWALD U, STRUSCH T, HALIM J, MAYERBERGER E, BARSOUM M W, FARLE M. Controlling the conductivity of Ti_3C_2 MXenes by inductively coupled oxygen and hydrogen plasma treatment and humidity [J]. Rsc Advances, 2017, 7: 13097−13103.

[35] FENG Ai-hu, YU Yun, WANG Yong, JIANG Feng, YU Yang, MI Le, SONG Li-xin. Two-dimensional MXene Ti_3C_2 produced by exfoliation of Ti_3AlC_2 [J]. Materials & Design, 2017, 114 161−166.

[36] ANDERSEN S Z, COLIC V, YANG S, SCHWALBE J A, NIELANDER A C, MCENANEY J M, ENEMARK-

RASMUSSEN K, BAKER J G, SINGH A R, ROHR B A, STATT M J, BLAIR S J, MEZZAVILLA S, KIBSGAARD J, VESBORG P C K, CARGNELLO M, BENT S F, JARAMILLO T F, STEPHENS I E L, NORSKOV J K, CHORKENDORFF I. A rigorous electrochemical ammonia synthesis protocol with quantitative isotope measurements [J]. Nature, 2019, 570: 504−508.

[37] YANG Jian-hua, BAI Hao-yuan, GUO Yan-zhen, ZHANG Han, JIANG Rui-bin, YANG Bao-cheng, WANG Jian-fang, YU J C. Photodriven disproportionation of nitrogen and its change to reductive nitrogen photofixation [J]. Angewandte Chemie-International Edition, 2020, 132: 2−12.

[38] LI Lai-quan, TANG Cheng, YAO Da-zhi, ZHENG Yao, QIAO Shi-zhang. Electrochemical nitrogen reduction: Identification and elimination of contamination in electrolyte [J]. ACS Energy Letters, 2019, 4: 2111−2116.

[39] MA Lei, CHENG Yi-sun, CAVATAIO G, MCCABE R W, FU Li-xin, LI Jun-hua. Characterization of commercial Cu-SSZ-13 and Cu-SAPO-34 catalysts with hydrothermal treatment for NH_3-SCR of NO_x in diesel exhaust [J]. Chemical Engineering Journal, 2013, 225: 323−330.

[40] KRESSE G, FURTHMULLER J. Efficiency of ab-initio total energy calculations for metals and semiconductors using a plane-wave basis set [J]. Computational Materials Science, 1996, 6: 15−50.

[41] KRESSE G, JOUBERT D. From ultrasoft pseudopotentials to the projector augmented-wave method [J]. Physical Review B, 1999, 59: 1758−1775.

[42] PAIER J, HIRSCHL R, MARSMAN M, KRESSE G. The perdew-burke-ernzerhof exchange-correlation functional applied to the G2-1 test set using a plane-wave basis set [J]. Journal of Chemical Physics, 2005, 122: 234102.

[43] GRIMME S, ANTONY J, EHRLICH S, KRIEG H. A consistent and accurate ab initio parametrization of density functional dispersion correction (DFT-D) for the 94 elements H-Pu [J]. Journal of Chemical Physics, 2010, 132: 154104.

[44] HOU Ting-ting, LI Qi, ZHANG Yi-da, ZHU Wen-kun, YU Kai-fu, WANG San-mei, XU Quan, LIANG Shu-quan, WANG Liang-bing. Near-infrared light-driven photofixation of nitrogen over $Ti_3C_2T_x/TiO_2$ hybrid structures with superior activity and stability [J]. Applied Catalysis B: Environmental, 2020, 273: 119072.

[45] PARK J, ALSHAMMARI F, WANG Z, ALSHAREEF H. Interface engineering for precise threshold voltage control in multilayer-channel thin film transistors [J]. Advanced Materials Interfaces, 2016, 3: 1600713.

[46] SUN Song-mei, WATANABE M, WU Ji, AN Qi, ISHIHARA T. Ultrathin $WO_3·0.33H_2O$ nanotubes for CO_2 photo-reduction to acetate with high selectivity [J]. Journal of the American Chemical Society, 2018, 140: 6474−6482.

[47] ZHENG Li-li, XIAO Xin-yan, LI Yang, ZHANG Wei-ping. Enhanced photocatalytic activity of TiO_2 nanoparticles using WS_2/g-C_3N_4 hybrid as co-catalyst [J]. Transactions of Nonferrous Metals Society of China, 2017, 27: 1117−1126.

[48] LIAO Yuan, QIAN Jing, XIE Gang, HAN Qing, DANG Wen-qiang, WANG Yuan-shen, LV Ling-ling, ZHAO Sen, LUO Lei, ZHANG Wen, JIANG Hai-ying, TANG Jun-wang. ration-layered Ti_3C_2 MXenes for promoted synthesis of NH_3 on P25 photocatalysts [J]. Applied Catalysis B: Environmental, 2020, 273: 119054.

[49] SHEN Chang-jie, WANG Li-bo, ZHOU Ai-guo, WANG Bo, WANG Xiao-long, LIAN Wei-wei, HU Qian-ku, QIN Gang, LIU Xu-qing. Synthesis and electrochemical properties of two-dimensional RGO/$Ti_3C_2T_x$ nanocomposites [J]. 2018, 8: 80.

[50] ZHANG Rui, DRYSDALE D, KOUTSOS V, CHEUNG R. Controlled layer thinning and p-type doping of WSe_2 by Vapor XeF_2 [J]. Advanced Functional Materials, 2017, 27: 1702455.

[51] HOU Ting-ting, XIAO Yu, CUI Pei-xing, HUANG Yi-ning, TAN Xiao-ping, ZHENG Xu-sheng, ZOU Ying, LIU Chang-xi, ZHU Wen-kun, LIANG Shu-quan, WANG Liang-bing. Operando oxygen vacancies for enhanced activity and stability toward nitrogen photofixation [J]. Advanced Energy Materials, 2019, 9: 1902319.

钨原子掺杂的 $Ti_3C_2T_x$ MXene 材料在全光谱氮气光固定中的应用

李 琪[1]，徐佶粱[1]，王三妹[1]，喻开富[2]，竹文坤[2]，侯婷婷[1]，张蓝天[1]，张文华[3]，梁叔全[1]，王梁炳[1]

1. 中南大学 材料科学与工程学院，长沙 410083；
2. 西南科技大学 环境友好型能源材料国家重点实验室，绵阳 621010；
3. 中国科学技术大学 材料科学与工程系 中国科学院能量转换材料重点实验室，合肥 230026

摘 要：将 W 原子掺杂到 $Ti_3C_2T_x$ MXene 材料中，成功制备具有全光谱氮气光固定催化活性的 W/$Ti_3C_2T_x$-U 光催化剂。在室温且无任何牺牲剂条件下，该催化剂作用下 NH_3 产率高达 228 μmol/(g·h)。对 W 掺杂及超声插层处理对 MXene 材料催化性能的影响进行研究。采用扫描透射电子显微镜、电子自旋共振波谱、X 射线光电子能谱、紫外−可见分光光度计、程序升温化学吸附分析仪及密度函数理论计算等多种方式对所得到的催化剂进行表征及研究。结果表明：$Ti_3C_2T_x$ Mxene 可收集紫外−可见光和近红外光以生成热电子；掺杂的 W 原子作为活性中心，向 N_2 分子的反键轨道贡献电子，使 N≡N 的键长增加，从而促进 N_2 分子的吸附和活化。

关键词：氮固定；光催化；MXene；钨；全光谱

(Edited by Xiang-qun LI)